

## WATER VAPOR IN THE SPECTRUM OF THE EXTRASOLAR PLANET HD 189733b: 1. THE TRANSIT

P. R. MCCULLOUGH<sup>1,2</sup>, N. CROUZET<sup>1,3</sup>, D. DEMING<sup>4,5</sup>, AND N. MADHUSUDHAN<sup>6,7</sup>

<sup>1</sup> Space Telescope Science Institute, Baltimore, MD 21218, USA

<sup>2</sup> Department of Physics and Astronomy, Johns Hopkins University, 3400 North Charles Street, Baltimore, MD 21218

<sup>3</sup> Dunlap Institute for Astronomy & Astrophysics, University of Toronto, 50 St. George Street, Toronto, Ontario, Canada M5S 3H4

<sup>4</sup> Department of Astronomy, University of Maryland, College Park, MD 20742, USA

<sup>5</sup> NASA Astrobiology Institute's Virtual Planetary Laboratory

<sup>6</sup> Yale Center for Astronomy & Astrophysics, Yale University, New Haven, CT 06511, USA and

<sup>7</sup> Institute of Astronomy, University of Cambridge, Madingley Road, Cambridge, CB3 0HA, UK.

(Received 2014 Feb 27; Accepted 2014 Jun 20)

Accepted for publication in the *Astrophysical Journal*

### ABSTRACT

We report near-infrared spectroscopy of the gas giant planet HD 189733b in transit. We used the *Hubble Space Telescope* Wide Field Camera 3 (*HST* WFC3) with its G141 grism covering  $1.1\ \mu\text{m}$  to  $1.7\ \mu\text{m}$  and spatially scanned the image across the detector at  $2''\text{s}^{-1}$ . When smoothed to 75 nm bins, the local maxima of the transit depths in the  $1.15\ \mu\text{m}$  and  $1.4\ \mu\text{m}$  water vapor features respectively are  $83 \pm 53$  ppm and  $200 \pm 47$  ppm greater than the local minimum at  $1.3\ \mu\text{m}$ . We compare the WFC3 spectrum with the composite transit spectrum of HD 189733b assembled by Pont et al. (2013), extending from  $0.3\ \mu\text{m}$  to  $24\ \mu\text{m}$ . Although the water vapor features in the WFC3 spectrum are compatible with the model of non-absorbing, Rayleigh-scattering dust in the planetary atmosphere (Pont et al. 2013), we also re-interpret the available data with a clear planetary atmosphere. In the latter interpretation, the slope of increasing transit depth with shorter wavelengths from the near infrared, through the visible and into the ultraviolet is caused by unocculted star spots, with a smaller contribution of Rayleigh scattering by molecular hydrogen in the planet's atmosphere. At relevant pressures along the terminator, our model planetary atmosphere's temperature is  $\sim 700$  K, which is below the condensation temperatures of sodium- and potassium-bearing molecules, causing the broad wings of the spectral lines of Na I and K I at  $0.589\ \mu\text{m}$  and  $0.769\ \mu\text{m}$  to be weak.

*Subject headings:* planetary systems – planets and satellites: atmospheres – techniques: spectroscopic – stars: individual (HD 189733)

### 1. INTRODUCTION

The K1V star HD 189733 hosts the transiting gas giant planet HD 189733b, at an orbital distance of 0.03 AU (Bouchy et al. 2005). In some ways this system is nearly optimally suited for study with transmission spectroscopy. Its short planetary orbital period (2.2 days), its great stellar brightness ( $K = 5.5$  mag), and its large planet-to-star radius ratio (0.15) combine for convenient observations of high sensitivity and high contrast. On the other hand, a significant negative is its intrinsic photometric variability,  $\sim 2\%$  peak to valley, due to rotational modulation of star spots (Aigrain et al. 2012). As such, it is photometrically more variable than  $\sim 95\%$  of stars in the Kepler sample (McQuillan et al. 2014; Ciardi et al. 2011; cf. also Figure 5 of McQuillan et al. 2012). As this paper will discuss, star spots complicate the interpretation of transmission spectra, including those of HD 189733b.

Transmission spectra provide a powerful means to detect molecular species in exoplanetary atmospheres due to the long path length of the stellar light through the planetary atmosphere (e.g. Brown et al. 2001; Seager & Sasselov 2000; Fortney et al. 2010). The differential transit depth of a molecular feature is directly proportional to the scale height of the atmosphere. For hot Jupiters, with high temperatures and low mean molecular weight (i.e.  $\text{H}_2$ -rich), the differential transit depth in specific molecular bands is large enough to be observable with existing instruments. In particular, water vapor has bands with large cross sections observable in the near in-

frared.

Upper limits or marginal detections have been reported of water in transmission for exoplanets HD 209458b (Barman 2007), XO-1b (Tinetti et al. 2010; Crouzet et al. 2012), and XO-2b (Crouzet et al. 2012). From *Spitzer* IRAC transit photometry at  $3.6\ \mu\text{m}$ ,  $5.8\ \mu\text{m}$ , and  $8\ \mu\text{m}$ , Tinetti et al. (2007) reported evidence of water vapor in the atmosphere of HD 189733b (but cf. Désert et al. 2009). The near-infrared transmission spectrum of HD 189733b in particular has garnered considerable attention, with the same NICMOS data being re-analyzed multiple times, with Swain et al. (2014) being the latest. The latter meta-analysis of the transmission spectra of Swain et al. (2008), Gibson et al. (2011), and Waldmann et al. (2013), predicted the amplitude of HD 189733b's  $1.4\ \mu\text{m}$  water vapor feature to be 300 ppm to 400 ppm. Other meta-analyses have been performed also (e.g. Madhusudhan & Seager 2009). Similarly, from ground-based *IRTF* near-infrared transmission spectra of HD 189733b, Danielski et al. (2014) reported water vapor features including ones at  $1.15\ \mu\text{m}$  and  $1.4\ \mu\text{m}$  with amplitudes at least twice those reported here.

Significant improvement has come with the *HST* instrument WFC3. Recently, Mandell et al. (2013) reported WFC3 observations of transits of WASP-12b, WASP-17b, and WASP-19b. Huitson et al. (2013) reported WFC3 observations of WASP-19b alone. Made under *HST* program 12181 (P.I. Deming), those observations preceded the development of spatial scanning and like prior observations, produced marginal detections or upper limits on the  $1.4\ \mu\text{m}$  water va-

por feature. Similar WFC3 spectra have been reported for WASP-12b observed in staring mode under *HST* programs 12230 (P.I. Swain; Swain et al. 2013) and 12473 (P.I. Sing; Sing et al. 2013). Coupling WFC3 to the new technique of spatially scanning the Hubble Space Telescope (*HST*) has enabled detections of water vapor in transmission spectra for HD 209458b, XO-1b, and HAT-P-1b under *HST* program 12181 (P. I. Deming) and now HD 189733b (program 12881; P. I. McCullough).

For some planets, clouds and/or haze can greatly affect our view of water vapor even if it exists in their atmospheres. Such is the case apparently for the smaller exoplanets GJ 1214b (Kreidberg et al. 2014) and GJ 436b (Knutson et al. 2014) that both exhibit featureless, flat spectra. Planets with no atmospheres, or insufficiently large scale heights of their atmospheres, would also present undetectably weak diagnostic spectral features in their atmospheres (Deming 2010). Even if molecular features are observed in a clear atmosphere, a degeneracy exists between the composition and the characteristic temperature of the region probed by the data, since the scale height is proportional to temperature. High resolution ( $R > 50$ ), high sensitivity data can place joint constraints on the composition and temperature simultaneously (e.g. Benneke & Seager 2012).

Due to their geometry of light rays grazing the terminator region (Fortney 2005), transmission spectra are more sensitive to clouds/haze and/or small atmospheric scale heights than day-side emission spectra, which have their own limitations. Grillmair et al. (2008) attributed to water a  $10 \mu\text{m}$  absorption feature in the emission spectrum of HD 189733b, and recently, Birkby et al. (2013) have done so at  $3.2 \mu\text{m}$  using phase curves rather than observations at secondary eclipse. Such measurements indicate potential for comparison of spectra obtained by the complimentary techniques of transits, eclipses, and phase curves (cf. Kreidberg et al. 2014 and Stevenson et al. 2014).

The spectral observations reported here were obtained in spatial scanning mode (McCullough & MacKenty 2012) with the *HST* in order to rapidly collect a large number of photons from HD 189733 without it also saturating the detector. In scanning mode, the *HST* scans across a small segment of a great circle on the sky while the detector is integrating photo-generated charge from objects as they trail across the detector. Since the first such observation of a transiting exoplanet, GJ 1214b on April 18, 2011 (program 12325, P.I. MacKenty; McCullough et al. 2012), spatial scanning has become the nominal method of spectroscopic observation of bright exoplanet host stars. Deming et al. (2013) scanned one transit each of HD 209458b and XO-1b; Kreidberg et al. (2014) and Knutson et al. (2014) each scanned multiple transits of GJ 1214b and GJ 436b respectively. Wakeford et al. (2013) scanned one transit of HAT-P-1b. *HST* program 12181 (P.I. Deming) recorded one transit of HD 189733b using spatial scans. However, the Earth occulted the telescope’s view of the star during the main part of the transit event between contacts 2 and 3.

Gibson et al. (2012) observed transits of HD 189733b in the near-infrared with WFC3, under program 11740 (P.I. Pont), although they did so prior to the advent of spatial scanning on *HST*. In those observations, the very bright star saturated the detector even before each exposure began, because the detector does not have a mechanical shutter. They salvaged light curves from the insensitive blue and red ends of the spectra. Based upon comparison of those measurements at  $\sim 1.1 \mu\text{m}$

and  $\sim 1.6 \mu\text{m}$  with measures by Pont et al. (2008) between  $0.5 \mu\text{m}$  and  $1.0 \mu\text{m}$ , Gibson et al. tentatively suggested that haze dominates the transmission spectrum of HD 189733b both in the visible and the near-infrared. However, they concluded that future observations of the sort reported here would provide the evidence to resolve the issue of whether exoplanetary hazes or clouds obscure spectral features in the near-infrared.

This paper is organized as follows. In Section 2 we describe the observations, which we analyze in Section 3. Results are in Section 4. We separately discuss star spots (§5) and the exoplanet’s atmospheric spectrum (§6), and the combination of the two (§7). We draw conclusions and summarize in Section 8.

## 2. OBSERVATIONS

*HST* program 12881 (McCullough, P.I.) was allocated five HST orbits to observe the transit of HD 189733b and five orbits to observe its eclipse. The eclipse observations are reported by Crouzet et al. (2014). In both cases, the event (transit or eclipse) occurs in the fourth of the five HST orbits. By design and common practice, the data from the first HST orbit is considered unreliable, as the telescope settles to its new thermal environment associated with a new orientation to the Sun after slewing to the target, and charge traps in the HgCdTe detector equilibrate to the unusual voltage associated with strong illumination. Discarding the data from the first orbit would leave two reliable HST orbits pre-transit, one in-transit, and one post-transit.<sup>1</sup>

We observed HD 189733b in transit with HST WFC3 on June 5, 2013 (Table 1). We used the G141 grism, to obtain slitless spectroscopy with spectral coverage from  $1.1 \mu\text{m}$  to  $1.7 \mu\text{m}$  at a resolution  $R = \lambda/\Delta\lambda = 130$  and a dispersion of  $4.7 \text{ nm pixel}^{-1}$  (Dressel 2014). In each HST orbit of the visit, we obtained a set of thirty-two 5.97-s exposures, each with the RAPID sample sequence of seven samples, and each with a  $512 \text{ pixel}$  by  $512 \text{ pixel}$  subarray. As noted in the Introduction, the spectra were obtained in spatial scanning mode. We interleaved scanning first forward and then reversing direction, obtaining sixteen forward-reverse pairs of exposures in each orbit. We had intended to locate the target on the detector such that its first-order spectrum would be entirely within a region read from a single amplifier; however we miscalculated and the 1st order spectrum crosses an amplifier boundary (at physical column 512) corresponding to  $\lambda = 1.55 \mu\text{m}$ . A similar miscalculation caused the spectrum to scan off the top of the subarray and hence some of the samples were lost.<sup>2</sup>

In the forward direction, samples 1 through 5 occur when HD 189733’s spectrum is on the subarray but during samples 6, 7, and 8 the spectrum is off the subarray and hence only the first four differences between samples are useful. In the reverse direction, samples 3 through 8 recorded HD 189733’s spectrum, and samples 1, and 2 were lost (Figure 1). The loss of 5 differences between samples of 14 total implies a loss in potential, Poisson-limited, signal-to-noise ratio of 20%.

We also obtained a direct image as the first exposure of the visit (Figure 1); the purpose of the direct image is to provide a high-resolution image to verify the location of the target with respect to any potentially contaminating stars in the same field

<sup>1</sup> Of the two separate analyses (§3), the N. C. one discarded data from the entire first orbit whereas the D. D. one discarded only the first eight scans of the first orbit.

<sup>2</sup> We adjusted the position for the eclipse observations (Crouzet et al. 2014).

of view. HD 189733 is a double star; the secondary is 4.0 magnitudes fainter in H band and is  $11.2''$  away from the primary at a PA of  $246^\circ$  (Bakos et al. 2006). There are a few stars closer to HD 189733A in projection than HD 189733B, but they are much fainter; in H band each is 1% to 2% of the brightness of HD 189733B, which itself is 2.5% of the brightness of HD 189733A. Because the nearby stars are so faint, and because our analysis technique isolates the spectrum of the target star in space and references it in time by dividing the in-transit spectrum by the out-of-transit spectrum, we expect any contributions of nearby stars to the transmission spectrum of the planet HD 189733b to be entirely negligible.

We needed to scan at  $\sim 2''\text{s}^{-1}$  to properly expose the detector and to avoid saturation. Also we wanted samples often enough to avoid overlapping the two spectra of the primary star HD 189733A and the secondary star HD 189733B,  $11.2''$  apart. Combined, those requirements imply sampling every  $\sim 5$  s, or faster. Of MULTIACCUM sequences currently available for WFC3, only the RAPID sequence sufficed.

The observational data are interleaved in time; 7 forward scan differences, each a 0.85-s exposure, followed by a 51 second gap as the scanning telescope reverses and the detector is prepared for the next exposure, followed by the 7 reverse scan-differences each one also 0.85-s long, and then a 51 second gap to return to the beginning of the pattern and to prepare the detector for the next forward-scan exposure. With two 6-s exposures every 114 s, the observational duty cycle would be 10.5%, although because only 9 of the 14 MULTIACCUM differences were useful, the duty cycle was 6.7%. In total, we obtained  $16 \times 9 \times 0.85 = 122$ -s of exposure in transit, which is only 3% of the transit's duration. The latter 3% is approximately half of the 6.7% observational duty cycle, because the Earth occulted the target during the second half of the transit. Rather unsatisfactorily, a 3% duty cycle with the 2.4-m *HST* would be equivalent to observing at 100% duty cycle with a 0.4-m diameter telescope of the same end-to-end throughput. Further improving WFC3's duty cycle by any practical operational changes would be beneficial for observations of stars such as HD 189733b.

### 3. ANALYSIS

Two of us (N.C. and D.D.) analyzed the data nearly independently. As planned from the outset to maintain independence, no computer code was shared between the two efforts, but both analysts had read or written the relevant literature, particularly descriptions by McCullough et al. (2012) Berta et al. (2012), Deming et al. (2013), Kreidberg et al. (2014), and Knutson et al. (2014). The two resulting exoplanetary transmission spectra were compared and found to be very similar. After discussions each analyst slightly revised his algorithms, which resulted in two final spectra. In this section, we described one analysis, that of N.C., the other method has been described already in its application to HD 209458 and XO-1 (Deming et al. 2013). Table 2 lists the transit light curve of the N.C. analysis. We describe the differences between the two analyses at the end of this section and list the difference between the two resulting spectra in the last column of Table 3. The r.m.s. of the differences, 52 ppm, is 0.75 times the median Poisson noise associated with the 4-column binning, indicating that the differences in the resulting binned spectra are statistically less significant than the physical limit imposed by Poisson statistics.

We begin the analysis with the set of Intermediate MultiAccum Flexible Image Transport System (ima.fits) files, which

are produced by the CALWFC3 pipeline at STScI and have a number of corrections applied, including dark current subtraction and nonlinearity correction (Rajan et al. 2011). As described in Section 2, we discard the data from the visit's first *HST* orbit. We sort the files into two sets, forward scans (keyword POSTARG2 = 54.9) and reverse scans (POSTARG2 = -2.0), and analyze each separately until combining them near the end of our analysis. The separate analyses of forward- and reverse-scans are very similar, differing only in the parameters defining the useful readouts and the pixels of interest, both of which differ slightly due to the forward and reverse scans not overlapping exactly.

From each 3-D multi-extension ima.fits file, we extract the difference images  $\Delta I_i$  corresponding to the  $i$ th difference of consecutive nondestructive reads of the detector subarray. We divide the 2-D difference images by a 2-D flat field obtained through the F139M filter. Because the in-transit spectrum of HD 189733 will be divided by its out-of-transit spectrum to form the planetary transmission spectrum, i.e. because the flat field is self-calibrated, the choice of particular flat-field is unimportant. Flat-fielding makes bad pixels and cosmic ray hits easier to identify. We perform such identification and accordingly correct the images by interpolation as described by Crouzet et al. (2014).

We define fixed regions on the 2-D images corresponding to the target's signal area and a corresponding sky area. We subtract the sky's value from each image. Next we sum each column over the stellar region, yielding a 1-D spectrum of HD 189733 for each difference image. We average those into in-transit spectra (IN, from the fourth *HST* orbit) and out-of-transit spectra (OUT, from three other *HST* orbits). We form each of nine planetary transit spectra, (OUT-IN)/OUT, associated with the nine difference images (four *forward* and five *reverse*), which we then average to form a single planetary spectrum, subtract the wavelength-integrated mean, and bin every four columns to produce the final, differential planetary spectrum (column 2 of Table 3).

We calibrated the wavelength as a function of detector column by comparing the (unbinned) WFC3 spectrum of HD 189733 to the spectrum of a K1 V comparison star (Rayner et al. 2009).<sup>3</sup> We adjusted the comparison star's spectrum to match HD 189733's spectrum by multiplying the comparison spectrum by the telescope and instrument throughput (Dressel 2014), transforming it from energy units to photo-electron units, smoothing it to 4.7 nm (1 column) resolution, high-pass filtering it and the WFC3 spectrum to emphasize weak spectral features in each, and finally, match the two spectra by linearly transforming the comparison star spectrum with an offset and dispersion that together constitute our wavelength calibration, which we estimate to be accurate to better than 4.7 nm (1 column). Additional details of this procedure are in Crouzet et al. (2014).

The position of the spectrum shifts slightly throughout each exposure in response to feedback from the fine guidance sensors. Variations in the scan rate perpendicular to dispersion introduce apparent photometric variations due to each row having a slightly shorter (longer) exposure time because the telescope's scan rate is faster (slower) than nominal (cf. Figure 1 of Deming et al. 2013). Because such variations are achromatic, they do not affect the differential exoplanetary spectrum. We also examined the shifts in telescope pointing parallel to dispersion by methods similar to those described

<sup>3</sup> [http://irtfweb.ifa.hawaii.edu/~spex/IRTF\\_Spectral\\_Library/Data/K1V\\_HD10476.txt](http://irtfweb.ifa.hawaii.edu/~spex/IRTF_Spectral_Library/Data/K1V_HD10476.txt)

in Deming et al. (2013). The peak-to-valley variation of the shifts throughout the visit of program 12881 was typical for *HST* (Gilliland 2005),  $\sim 0.1$  column ( $\sim 0.014''$ ), similar to that for XO-1 and much less than the  $\sim 1.0$  column shift of HD 209458b, both observed in program 12181 (cf. Figure 4 of Deming et al. 2013). Adjusting the spectra of HD 189733 for its small ( $\lesssim 0.1$  column) shifts made negligible difference in the final exoplanet spectrum compared to not making the adjustments.<sup>4</sup>

An important difference between the two analyses is their smoothing. The analysis of D. D. smoothed its spectrum with a Gaussian of FWHM=4 columns whereas the other one, of N. C., used a box-car smoothing of full width 4 columns. Purely as a consequence of the choice of smoothing kernels, for an idealized, featureless, flat power spectrum of noise in the unbinned spectrum, the ratio of the noise of the resulting smoothed spectra should be  $\sigma_{D.D.}/\sigma_{N.C.} = \sqrt{\pi/\sqrt{32\ln 2}} = 0.817$ . Stated another way, in terms of noise power, the D. D. spectrum has an effective bin width of 6 columns, or 1.5 times the N. C. spectrum’s 4-column bin width.<sup>5</sup> The uncertainties in Table 3 match this expectation.

## 4. RESULTS

### 4.1. Light Curve

We subdivided the available WFC3 data into nine separate wavelength-integrated “white light” curves, corresponding to the nine differences between MULTIACCUM samples in which HD 189733 was on the subarray. Figure 2 illustrates one example of the nine available. We removed trends in each light curve as follows, for each of the nine MULTIACCUM differences separately. We fit a straight line by least-squares to the first points of the second, third, and fifth *HST* orbits, and divided the first point of each *HST* orbit (including the in-transit fourth orbit) by the fit. We repeated the procedure for the second point, and so on, for all thirty-two scans per *HST* orbit. Table 2 lists the nine light curves, both before and after de-trending.

From the light curve of HD 189733b’s transit we obtain the mean level of the transit depth  $R_p^2/R_s^2$ , which is important for comparison with measurements at other wavelengths from other instruments. Otherwise, however, we are not as interested in the light curve as the differential transit spectrum described in the next section. We adopted HD 189733b’s ephemeris, orbital inclination, and normalized semi-major axis from Knutson et al. (2012). We fit the light curve with the procedure of Mandel & Agol (2002), using quadratic limb darkening coefficients  $u_1 = 0.1378$  and  $u_2 = 0.232$ , which we derived by fitting two parameters of a quadratic law to the three-parameter limb-darkening law adopted by Sing et al. (2009) for  $\lambda = 1.66 \mu\text{m}$ . The resulting mean transit depth, appropriate for the integrated WFC3 bandpass, is  $R_p^2/R_s^2 = 0.024332 \pm 0.0001$ , where the estimated uncertainty (100 ppm) is the standard deviation of the fits to the nine light curves. The observed value of  $R_p^2/R_s^2$  is an upper bound in so far as it neglects unocculted star spots (cf. §5).

<sup>4</sup> The analysis of D. D. included such adjustments; the analysis of N. C. did not.

<sup>5</sup> To derive the factor, recall that the convolution of a Gaussian is another Gaussian in the Fourier-transformed space, and via Parseval’s theorem, noise power is equal in both one space and the space of its Fourier conjugate. We also verified the value of 0.817 by numerical simulation.

### 4.2. Exoplanet Transmission Spectrum

The exoplanet transmission spectrum is the transit depth  $R_p^2/R_s^2$  as a function of wavelength. In column 2 of Table 3 we report the differential transmission spectrum as (IN-OUT)/OUT, with its mean value subtracted, where IN is the mean in-transit spectrum (from the fourth *HST* orbit) and OUT is the mean out-of-transit spectrum (from the other *HST* orbits, neglecting the first one). Figure 3 illustrates the spectrum extending from  $1.13 \mu\text{m}$  to  $1.64 \mu\text{m}$  in 28 bins. Each bin corresponds to 19 nm or four detector columns. The simple (IN-OUT)/OUT estimate neglects limb darkening. Our more complicated analysis (Deming et al. 2013) involves subtracting a scaled template spectrum from each exposure’s 1-D spectrum and then fitting a transit light curve to the residuals to derive the differential transit depth at each wavelength. In the latter method, limb darkening can be included or not, and we experimented with either choice. Although the mean “white light” transit depth is sensitive to the limb-darkening correction, applying a wavelength-dependent limb-darkening correction, or not, made negligible difference to the differential transit depth. To emphasize the latter point, we computed one differential spectrum with no limb-darkening correction at all (column 2 of Table 3), although we did model limb-darkening for the white-light transit depth in the previous section.

We estimated the uncertainties in column 3 of Table 3 as follows. We formed an individual 1-D stellar spectrum from each difference image. We form a template spectrum from data taken out-of-transit. We then scale and subtract the template from each of the individual spectra in order to minimize the r.m.s. of the resulting residuals. For each spectral channel, we group the residuals into two sets, one in-transit and one out-of-transit, divide by the mean flux, and evaluate their respective standard deviations  $\sigma_{in}(\lambda)$  and  $\sigma_{out}(\lambda)$ . We combine the latter in quadrature, accounting for the number of measurements in-transit or out-of-transit respectively, in order to estimate the uncertainties of each spectral channel,  $\sigma(\lambda)$ .

In Figure 4 we bin the data from column 2 of Table 3 into seven points, with a channel width of 75 nm (16 detector columns). With that smoothing, the local maxima of the transit depths in the  $1.15 \mu\text{m}$  and  $1.4 \mu\text{m}$  water vapor features occur at the first and fourth data points, with a local minimum, the third point, in between. From those, we estimate the amplitudes of the  $1.15 \mu\text{m}$  and  $1.4 \mu\text{m}$  features respectively are  $83 \pm 53$  ppm and  $200 \pm 47$  ppm greater than the local minimum at  $1.3 \mu\text{m}$ . The stated uncertainties are the quadrature sum of the uncertainties of the two points in each case. The  $1.4 \mu\text{m}$  feature in particular is detected at much greater statistical significance than  $\sim 4\sigma$ , i.e.  $200/47$ , because the feature extends over two 75-nm wide points and the adjacent baseline extends over two or four points instead of just one. By averaging over four points, two inside the  $1.4 \mu\text{m}$  feature and the two adjacent to it, the  $\sim 4\sigma$  result becomes  $\sim 8\sigma$ , commensurate with the feature’s appearance in Figures 4 and 5.

The peak-to-valley amplitude of the  $1.4 \mu\text{m}$  feature in Figure 3, which has spectral resolution of 30 nm FWHM in the model or 19 nm (4 columns) in the binned data, is  $\sim 400$  ppm or  $\sim 350$  ppm, respectively. The peak-to-valley measurement of a noisy spectrum depends on the smoothing that reduces noise and hence reduces the height of the peak and the depth of the valley. The similarity of the model to the data in Figure 3 illustrates that the data are consistent with a clear-atmosphere of solar-composition, with a volume mixing ratio

for water of  $\sim 5 \times 10^{-4}$  and a pressure scale height commensurate with a temperature of 700 K. The  $\sim 5 \times 10^{-4}$  mixing ratio has been used in prior models as well (e.g. Tinetti et al. 2007, Swain et al. 2008, Danielski et al. 2014) and is consistent with the broad range of values presented in Figure 3 of Swain et al. (2014),  $\sim 1 \times 10^{-4}$  to  $\sim 1 \times 10^{-2}$ . However, inspection of Figure 3 shows that slightly reducing our model’s amplitude would improve its fit to the data. Hence, either the volume mixing ratio or the temperature should be smaller than the assumed values. Madhusudhan et al. (2014) explore the fitting of these data in greater detail and conclude that the H<sub>2</sub>O volume mixing ratio is sub-solar.

### 5. STAR SPOTS

HD189733 is an active star (Boisse et al. 2009), and transit observations exhibit ubiquitous star spot crossings (Pont et al. 2007). Our WFC3 observations have only partial coverage during transit because of occultation by the Earth, and no spot crossings are obvious in our data. In any case, because HD 189733 is a spotted star, we must address two effects *unocculted* star spots may have on the transmission spectrum. First, unocculted star spots can make the radius of a transiting planet appear larger in the blue than in the red, because unocculted spots make the star darker and redder than it would appear otherwise. If in fact a star is *darker* away from the transit chord than a model assumes, that model will overestimate the size of the transiting planet. If in fact the star is also *redder* away from the transit chord than the model assumes, then the overestimate of the planet’s size will be even greater in the blue than in the red. Second, at  $T_{eff} = 5000\text{K}$ , HD 189733’s photosphere is too hot for water to exist, but in very cool star spots, water vapor could exist. Water vapor absorption in unocculted star spots will make the star spots darker in spectral features of water than in the continuum, and hence make the radius of the transiting planet appear larger in water-vapor features than it would in the continuum (Deming et al. 2013). Quantitatively and specifically for HD 189733, we show in this section that the first effect is likely to be significant but the second effect is not.

Pont et al. (2013) analyze star spots on HD 189733 and their potential effects on the transmission spectrum. In their analysis, they show that star spots modulate the stellar flux primarily due to stellar rotation, and also due to the changing set of spots and their characteristics. However, latitudinal *bands* of star spots would not modulate the flux much, because as one spot rotates into view, another one rotates out of view.<sup>6</sup> If HD 189733 has a large polar spot, or one or more latitudinal band(s) of spots beyond the latitudes at which the transit chord passes, then those unocculted spots will contribute to the apparent rise in the “planetary” transmission spectrum seen in the visible with ACS (Pont et al. 2008) and in the ultraviolet with STIS (Sing et al. 2011). Pont et al. (2013) were aware of such possibilities but chose to interpret that rise in the spectrum as evidence of Rayleigh-scattering dust in the planet’s upper atmosphere instead of spots on the star. In this paper we match all of the transit data assembled by Pont et al. (2013) and the WFC3 spectrum derived here with a combination of a clear planetary atmosphere and a spotted stellar photosphere.

As in prior work (e.g., Pont et al. 2008, 2013; Sing et al.

<sup>6</sup> From observations of the Rossiter-McLaughlin effect for HD 189733b, we know that the stellar rotation axis is in the plane of the sky (Triaud et al. 2009).

2011), we model star spots in aggregate and ignore limb darkening. In the spotted-star model, a fraction  $\delta$  of the star’s projected surface area is covered with spots, emitting with radiance  $F_V(\text{spot})$ , less than that of the photosphere,  $F_V(\text{phot})$ . Such a model predicts an apparent transit depth,

$$\frac{\tilde{R}_p^2}{\tilde{R}_s^2} = \frac{R_p^2}{R_s^2} \frac{1}{1 - \delta(1 - F_V(\text{spot})/F_V(\text{phot}))}, \quad (1)$$

where the first factor on the right is the transit depth that would be measured in the absence of star spots.

Aigrain et al. (2012) used simulated, rotating spotted stars modeled on HD 189733 to estimate the product of its spots’ area coverage  $\delta$  and (1-contrast),

$$f = \delta(1 - \text{contrast}) \approx \frac{\Psi_{\max} - \Psi_{\min} + \sigma}{\Psi_{\max} + \sigma}, \quad (2)$$

where  $\Psi_{\max} - \Psi_{\min}$  is the difference in the stellar flux from maximum to minimum, and  $\sigma$  is the scatter in the light curve, also due to rotational modulation (not observational uncertainty). From six years of photometry at  $\lambda = 0.51 \mu\text{m}$  of HD 189733 illustrated in Figure 3 of Pont et al. (2013), we estimate  $\Psi_{\max} - \Psi_{\min} \approx 0.04\Psi_{\max}$  and hence  $f$  can be comparable to, or larger than, 0.04. Because  $f$  represents the product, spot area times (1-contrast), and contrast must be less than unity, in general, the fraction  $\delta$  of the star’s disk covered with spots must be greater than  $f$ . Thus, for HD 189733, we expect  $\delta$  at times is greater than approximately 0.04. A caveat worth noting is that the analysis of Aigrain et al. (2012) is most appropriate for stars for which a single active region dominates the photometric variability. Also, as noted by Aigrain et al. (2012), geometric foreshortening de-emphasizes the contribution to the rotational modulation of spots near the stellar limb. With those caveats in mind, we admit the possibility that Equation 2 underestimates  $f$  and hence  $\delta$  could be even larger than 0.04, if for instance HD 189733 has many active regions spread uniformly in longitude, i.e. bands of star spots.

The values of Pont et al. (2013), which we use as a starting point in our analysis, have been corrected already for unocculted star spots that modulate the light curve, with time-dependent “AC” values for  $\delta$  corresponding to flux changes in the optical between  $-0.93\%$  and  $+1.47\%$  (Table 3 of Pont et al. 2013). The most important corrections are to the ACS and STIS data, because the transmission spectrum at wavelengths longer than  $\sim 1 \mu\text{m}$  are less affected by the unocculted spot correction and/or by the Rayleigh-scattering dust model (Figures 4 and 5). The unocculted spot corrections derived by the procedure of Pont et al. (2013) produced a discontinuity between the STIS and ACS transmission spectra in the region of overlap at  $\sim 0.5 \mu\text{m}$ . To eliminate the discontinuity, they applied a smaller correction than their method had indicated for unocculted spots at the epoch of the STIS observations. While Pont et al. (2013) have corrected for an AC component, here we investigate an underlying “DC” component and its potential effects on the transmission spectrum. The DC component is an additional, hypothetical set of unocculted spots in bands or a polar cap. With either such configuration, they would not modulate the light curve or precision radial velocities either. Polar spots have been deduced from Doppler imaging of rapidly rotating stars, e.g. the K0 dwarf AB Dor has a rotation period of 0.5 days and exhibits a prominent, long-lived polar spot (Collier Cameron 1995), but we know little about the spots of more slowly-rotating stars such as HD 189733.

### 5.1. Black Body models

Before proceeding to the more realistic PHOENIX atmosphere models, we begin with the approximation of black bodies for the stellar photosphere and the star spots, at temperatures  $T_{phot}$  and  $T_{spot}$  respectively. In this approximation, Equation 1 becomes

$$\frac{\bar{R}_p^2}{\bar{R}_s^2} = \frac{R_p^2}{R_s^2} \frac{1}{1 - \delta \left(1 - \frac{e^{h\nu/kT_{phot}} - 1}{e^{h\nu/kT_{spot}} - 1}\right)}, \quad (3)$$

where  $h$  is Planck's constant,  $k$  is Boltzmann's constant, and  $\nu$  is the observing frequency. The spots' multiplicative effect on the apparent transit depth as a function of wavelength asymptotically approaches one value in the Wien limit (in the ultraviolet) and another in the Rayleigh-Jeans limit (in the far infrared):

$$\frac{\bar{R}_p^2}{\bar{R}_s^2} = \frac{R_p^2}{R_s^2} \frac{1}{1 - \delta}, \quad \text{Wien} \quad (4)$$

$$= \frac{R_p^2}{R_s^2} \frac{1}{1 - \delta \left(1 - T_{spot}/T_{phot}\right)}, \quad \text{Rayleigh - Jeans.} \quad (5)$$

The difference between the two limits is

$$\Delta \frac{\bar{R}_p^2}{\bar{R}_s^2} = \frac{R_p^2}{R_s^2} \left( \delta \frac{T_{spot}}{T_{phot}} + O(\delta^2) \right), \quad (6)$$

$$\approx 960 \frac{\delta}{0.04} \frac{T_{spot}}{T_{phot}} \text{ ppm}, \quad (7)$$

where the first expression is generic and the second is specific for HD 189733b's nominal transit depth of 2.40%. Intuitively, the greater the fractional area of star spots,  $\delta$ , the greater the increase in apparent transit depth in the ultraviolet relative to the thermal infrared. Counter-intuitively (perhaps), the cooler the spots, the less their effect on the difference in apparent transit depth  $\Delta \frac{\bar{R}_p^2}{\bar{R}_s^2}$ . This is because in the Wien limit, the radiance of cool spots is arbitrarily smaller than that of the photosphere, i.e. the spots are essentially black silhouettes, whereas in the Rayleigh-Jeans limit, radiance is proportional to temperature, so the *difference* in radiances (Rayleigh-Jeans minus Wien) is proportional to the ratio of temperatures, and then so is the difference in apparent transit depth.

These characteristics of blackbodies inform our expectations for the effect of unocculted spots on the apparent transit depth. Pont et al. (2008) estimate that  $T(\text{spot}) \sim 4000\text{K}$ , and Sing et al. (2011) find  $T(\text{spot}) = 4250 \pm 250\text{K}$  for HD 189733. If the typical spot covering fraction  $\delta$  is approximately 4%, then Equation 7 predicts the difference in apparent transit depth between the ultraviolet and the infrared should be  $\sim 800$  ppm, entirely due to unocculted star spots and not due to any variation in planetary radius with wavelength. From Table 6 of Pont et al. (2013), the observed difference in transit depth between  $0.33\ \mu\text{m}$  and  $24\ \mu\text{m}$  is 1100 ppm. Evidently, a majority fraction of the increased apparent transit depth in the ultraviolet compared to the infrared could be due to *more* unocculted star spots than that assumed by Pont et al. (2013). If so, then there would be no need for Rayleigh-scattering, non-absorbing dust in the atmosphere of HD 189733b in order to match the slope in the apparent transit depth with wavelength from  $0.3\ \mu\text{m}$  to  $1.0\ \mu\text{m}$  as in the interpretation of Pont et al. (2013).

### 5.2. PHOENIX models

To achieve greater fidelity than the black body models permit, we have modeled the effect of unocculted star spots using Phoenix NextGen model atmospheres (Hauschildt et al. 1999). We use a 5000/4.5/0.0 (Teff/log(g)/[M/H]) model for the star, and for the spots we use NextGen models whose temperature we vary between 3000 and 5000K, in steps of 50 K via interpolation in the NextGen grid. We constrain the log(g) and metallicity of the spots to be the same as the stellar model, and we ignore center-to-limb effects on the star spot spectrum. This procedure is consistent with similar previous work (e.g., Pont et al. 2008, 2013; Sing et al. 2011). At each adopted spot temperature, we vary the assumed fractional area covered by the spots, and we calculate the effect on the transit depth as a function of wavelength (Equation 1).

We calculate the  $\chi^2$  of the difference between the modeled transit depth as a function of wavelength, using the observations in Table 5 of Pont et al. (2013). To start, we adopt the limiting-case in which all of the observed planetary radius increase in the blue and UV is due to unocculted star spots and the spot-free radius ratio  $R_p/R_s$  is 0.15459, from the longest wavelength transit measurement at  $24\ \mu\text{m}$  (Knutson et al. 2009; Pont et al. 2013). In that case we find a best-fit spot temperature of 4250K and a best-fit area coverage of 4.3%. This fitting process is well-posed in the sense that the wavelength of the upward bend in the curve is determined by the temperature adopted for the star spots (the cooler the spots, the longer the wavelength), and the difference in apparent transit depth from the Rayleigh-Jeans end to the Wien end of the curves is proportional to the product of the spots' temperature and area coverage (Equation 7).

Our best-fit temperature agrees well with spot temperatures inferred from the amplitudes of spot crossings by this planet; Pont et al. (2008) find that  $T_{spot} \sim 4000\text{K}$ , and Sing et al. (2011) find  $T_{spot} = 4250 \pm 250\text{K}$ . Our best-fit model predicts  $\delta = 0.043$ , similar to the value  $f = 0.04$  that we estimated from the spot modulation of HD 189733's light curve at  $\lambda = 0.51\ \mu\text{m}$ . In this case, the contamination of the  $1.4\ \mu\text{m}$  water-vapor feature is negligible, as we now discuss.

The model exhibits no spectral feature due to water absorption in the unocculted star spots, since 4250K is too warm for significant water absorption to be present. Hence even the worst-case assumption that all of the transit radius measurements are due to star spots does not produce significant contamination of the WFC3 water spectrum. That remains true if a much cooler spot temperature (3200K) is adopted, for example. Such a spot is much cooler than the estimates noted in the previous paragraph, and is also cooler than much larger spots seen on other stars (O'Neal et al. 1998). Moreover, even spots of  $T = 3200\text{K}$  do not produce sufficient water absorption to contaminate our WFC3 measurement; the predicted amplitude of false water absorption is  $\sim 40$  ppm - much less than the  $\sim 200$  ppm feature at  $1.4\ \mu\text{m}$  that we measure. We conclude that our WFC3 measurement of water absorption is due to the planetary atmosphere, not to an effect of unocculted star spots.

## 6. PLANET ATMOSPHERE MODELS

We constrain the  $\text{H}_2\text{O}$  abundance from our observed transmission spectra of HD 189733b using model atmospheric spectra of its terminator. We use the atmospheric modeling and retrieval technique of Madhusudhan & Seager (2009) and Madhusudhan (2012). The model involves computing line-

by-line radiative transfer in a 1-D plane-parallel atmosphere, assuming hydrostatic equilibrium. The temperature profile and chemical composition are free parameters in the model, and, as such, has no constraints of radiative or chemical equilibrium. This modeling approach allows one to compute large ensembles of models ( $\sim 10^6$ ), and explore the parameter space of molecular compositions and temperature structure in search of the best-fitting models. Typically, the model includes opacity contributions from the major molecular species expected in hot Jupiter atmospheres (i.e.  $\text{H}_2$ - $\text{H}_2$  collision-induced absorption and line absorption due to  $\text{H}_2\text{O}$ ,  $\text{CO}$ ,  $\text{CH}_4$ , and  $\text{CO}_2$ ), though  $\text{H}_2\text{O}$  is the most dominant molecule spectroscopically in the WFC3 bandpass. The transmission spectrum is less sensitive to the detailed temperature structure, compared to a thermal emission spectrum, but does depend on the characteristic temperature in the upper-atmosphere above the infrared photosphere when viewed through the terminator. In the present work, we assume a characteristic 1-D temperature profile that has been derived from thermal emission measurements in the past (Madhusudhan & Seager 2009), and explore the range of chemical compositions that explain the transit data.

We find that our WFC3 transmission spectrum of HD 189733b can be explained very well by  $\text{H}_2\text{O}$  absorption at the terminator. The WFC3 spectrum exhibits an absorption feature at  $1.4 \mu\text{m}$  with an amplitude of  $\sim 200$  ppm that coincides with the expected features of gaseous  $\text{H}_2\text{O}$  in the same band. As shown in Fig. 3, the data can be fit well by a solar composition atmosphere in chemical equilibrium. Such an atmosphere has a  $\text{H}_2\text{O}$  mixing ratio of  $\sim 5 \times 10^{-4}$ , where the mixing ratio is defined as number density relative to  $\text{H}_2$ . At the pressures probed by the observations ( $P \lesssim 0.1$  bar), the temperature profile has typical isothermal temperature of  $\sim 700$  K, slightly cooler than prior P-T curves used to model NICMOS transmission spectra of HD 189733b's terminator and its day-side emission spectrum from *Spitzer* (c.f. Figures 5 and 8 of Madhusudhan & Seager 2009). In principle, allowing for higher temperatures (e.g. 1000 K) leads to larger scale heights thereby constraining the  $\text{H}_2\text{O}$  abundance to be slightly sub-solar ( $\lesssim 10^{-4}$ , Madhusudhan et al. 2014). Nevertheless, the evidence of an absorption feature in the  $\text{H}_2\text{O}$  band is unambiguous, despite the degeneracy between the characteristic temperature and the  $\text{H}_2\text{O}$  mixing ratio. A featureless flat spectrum does not fit the data, ruling out the possibility of thick clouds fully obscuring the atmosphere observable along the planet's terminator. On the other hand, a fully-obscuring cloud deck at lower altitudes (i.e. higher pressures,  $\gtrsim 0.1$  bar) in the atmosphere is not ruled out by these WFC3 data.

#### 7. COMBINED PLANETARY ATMOSPHERE AND STAR-SPOT MODELS

Combining our WFC3 spectrum of HD 189733b with previously reported spectra in other bandpasses reveal new constraints on its atmospheric composition. The sum-total of previous data have led to an interpretation of hazes or clouds in the atmosphere of the planet (Pont et al. 2008; Sing et al. 2011; Pont et al. 2013). In Figure 5 we present a model that combines the effects a clear planetary atmosphere and unocculted star spots. For the gas giant planet, we model a clear atmosphere of solar composition, a mixing ratio for water of  $5 \times 10^{-4}$ , and zero alkali metal lines (Na and K). The Rayleigh scattering of  $\text{H}_2$  in the planetary atmosphere contributes significantly at wavelengths less than 0.5 microns. Incidentally, that scattering may be responsible for the higher

geometric albedo for the day side of HD 189733b observed at short wavelengths,  $\lambda < 0.45 \mu\text{m}$ , than at longer wavelengths,  $\lambda > 0.45 \mu\text{m}$  (Evans et al. 2013). Because the STIS spectrum ( $\lambda < 0.5 \mu\text{m}$ ) has a Rayleigh-scattering slope, the star spot contribution must saturate in order that the model spectrum not rise too quickly into the ultraviolet. That is accomplished with a cool, 3700 K spot temperature. The star's model is a PHOENIX atmosphere model for the 5000 K stellar photosphere with unocculted spots of temperature  $T(\text{spot}) = 3700$  K and spot fractional area  $\delta = 0.056$ . Although it fits the available data well, the combined model presented here is not unique: it is one example of many possibilities. As another example that could fit the transmission spectrum of HD 189733b is an "enhanced Rayleigh" model proposed for WASP-12b by Sing et al. (2013) in which the planet's atmosphere has both Rayleigh scattering from aerosols and water vapor absorption. A main purpose of this paper is to emphasize that fitting any transmission spectrum with a planetary atmosphere model must also consider the potential contribution and complication of unocculted star spots.

In prior work, the case for haze/clouds in the atmosphere of the planet has been based on three key arguments: (1) The monotonic rise in the spectrum from the near-infrared to the UV consistent with strong Rayleigh and Mie scattering, (2) the lack of strong Na or K features in the optical spectrum, i.e. presumably masked by a thick haze layer, and (3) the lack of striking  $\text{H}_2\text{O}$  absorption in previous datasets. We are able to explain the monotonic blue-ward rise in the transmission spectrum by considering the effect of star spots on the measured transit depths in the relevant wavelengths (Section 5). Secondly, the lack of Na and K features in optical transmission spectra could be explained by either a low metallicity in the atmosphere (Huitson et al. 2012) and/or by condensation of Na and K either in the low-temperature upper atmosphere or on the night side. The latter model is a distinct possibility, given that HD 189733b is one of the least irradiated hot Jupiters ( $T_{\text{eq}} \sim 1200$  K). Fortney et al. (2005) and Morley et al. (2013) show the condensation curves of various species in pressure-temperature phase space. At  $P \sim 1$  bar, condensation temperatures of KCl and  $\text{Na}_2\text{S}$  are  $\sim 800$  K and  $\sim 1000$  K, respectively, which can be higher than the temperatures in HD 189733b at the corresponding pressure on the terminator. Consequently, Na and K could be condensed out of the observable atmosphere by arbitrarily large factors into their corresponding compounds (e.g. KCl,  $\text{Na}_2\text{S}$ ). Finally, the  $\sim 200$  ppm amplitude of the  $1.4 \mu\text{m}$  feature reported here (and also in other exoplanets; see §1) explains why it was not as obvious in previous datasets as had been anticipated.

#### 8. SUMMARY

We report detection of two water vapor features in the transmission spectrum of HD 189733b, a strong one at  $1.4 \mu\text{m}$  and a weaker one at  $1.15 \mu\text{m}$ . Their shapes and amplitudes are matched well by a solar-composition planetary atmosphere with a water mixing ratio of  $5 \times 10^{-5}$ . We investigate the possibility that the water vapor could exist in star spots, but even for very cool spots ( $T = 3200$  K), the amplitude of the predicted  $1.4 \mu\text{m}$  feature is much too small to produce the observed feature.

The ensemble, polychromatic transit spectrum of HD 189733b, from the ultraviolet to the thermal infrared, has been interpreted by Pont et al. (2013), and references therein, as evidence for Rayleigh scattering in the planetary atmosphere. That interpretation requires specific adjustments for unoc-

culted star spots in order to match the transmission spectrum across the entirety of the ultraviolet and visible. We re-interpret the polychromatic transit spectrum using a clear planetary atmosphere and unocculted star spots. In the model presented here, Rayleigh scattering in a clear planetary atmosphere contributes significantly to the slope in the planetary radius as function of wavelength for  $0.3\mu\text{m} < \lambda < 0.5\mu\text{m}$ . In the range  $0.5\mu\text{m} < \lambda < 1.0\mu\text{m}$ , the observed slope is caused by unocculted star spots, not the planetary atmosphere. Since Rayleigh scattering by transparent dust grains in the planetary atmosphere has been central to prior interpretations of HD 189733b's transmission spectra, our modeling of a clear planetary atmosphere and a spotted stellar atmosphere is a significant revision in the interpretation. Given the complexities of stitching together data from different instruments observing transits of a variable star at different epochs, and given the potential of omnipresent star spots to further confuse matters, either the star spot interpretation or the Rayleigh scattering interpretation, or some combination of the two, remain viable. Prior work has rejected clear planetary atmosphere models based upon the predicted large-and-broad alkali metal lines in transmission spectra, Na I ( $0.589\mu\text{m}$ ) and K I ( $0.769$

$\mu\text{m}$ ) (Fortney et al. 2010). In our model, the strengths of those features are reduced by arbitrarily large amounts because Na and K are expected to precipitate out (Fortney et al. 2005; Morley et al. 2013) at the low temperatures ( $\sim 700\text{K}$ ) that we used to model the  $\sim 200$  ppm amplitude of the water vapor feature at  $1.4\mu\text{m}$ .

The authors gratefully acknowledge everyone who has contributed to the *Hubble Space Telescope* and the WFC3, and particularly those responsible for implementing the spatial scanning, which was critical to these observations. We thank in particular John MacKenty and Merle Reinhart. We acknowledge conversations with Suzanne Aigrain, David Ciardi, Suzanne Hawley, Leslie Hebb, Veselin Kostov, Rachel Osten, Frederic Pont, Neill Reid, and David Sing.

This research used NASA's Astrophysics Data System Bibliographic Services, and the SIMBAD database, operated at CDS, Strasbourg, France, and was funded in part by *HST* grant GO-12881 and Origins of Solar Systems grant NNX10AG30G.

## REFERENCES

- Agol, E., Cowan, N. B., Knutson, H. A., et al. 2010, *ApJ*, 721, 1861  
 Aigrain, S., Pont, F., & Zucker, S. 2012, *MNRAS*, 419, 3147  
 Bakos, G. Á., Pál, A., Latham, D. W., Noyes, R. W., & Stefanik, R. P. 2006, *ApJ*, 641, L57  
 Barman, T., 2007, *ApJ*, 661, L191.  
 Benneke, B., & Seager, S. 2012, *ApJ*, 753, 100  
 Berta, Z. K., Charbonneau, D., Désert, J.-M., et al. 2012, *ApJ*, 747, 35  
 Birkby, J. L., de Kok, R. J., Brogi, M., et al. 2013, *MNRAS*, 436, L35  
 Boisse, I., Moutou, C., Vidal-Madjar, A., et al. 2009, *A&A*, 495, 959  
 Bouchy, F., Udry, S., Mayor, M., et al. 2005, *A&A*, 444, L15  
 Brown, T. M., 2001, *ApJ*, 553, 1006.  
 Ciardi, D. R., von Braun, K., Bryden, G., et al. 2011, *AJ*, 141, 108  
 Collier Cameron, A. 1995, *MNRAS*, 275, 534  
 Crouzet, N., McCullough P. R., Burke, C., & Long, D., 2012, *ApJ*, 761, id.7.  
 Crouzet, N., McCullough P. R., Deming, D. & Madhusudhan, N. 2014, *ApJ*, in press  
 Danielski, C., Deroo, P., Waldmann, I. P., Hollis, M. D. J., Tinetti, G. & Swain, M. R. 2014, *ApJ*, 785, 35  
 Deming, D. 2010, *Nature*, 468, 636  
 Deming, D., Wilkins, A., McCullough, P., et al. 2013, *ApJ*, 774, 95  
 Désert, J.-M., Lecavelier des Etangs, A., Hébrard, G., et al. 2009, *ApJ*, 699, 478  
 Dressel, L. 2014, *Wide Field Camera 3, HST Instrument Handbook, Version 6.0* (Baltimore: STScI)  
 Evans, T. M., Pont, F., Sing, D. K., et al. 2013, *ApJ*, 772, L16  
 Fortney, J. J. 2005, *MNRAS*, 364, 649  
 Fortney, J. J., Marley, M. S., Lodders, K., Saumon, D., & Freedman, R. 2005, *ApJ*, 627, L69  
 Fortney, J. J., Shabram, M., Showman, A. P., et al. 2010, *ApJ*, 709, 1396  
 Gibson, N. P., Pont, F., & Aigrain, S. 2011, *MNRAS*, 411, 2199  
 Gibson, N. P., Aigrain, S., Pont, F., et al. 2012, *MNRAS*, 422, 753  
 Gilliland, R. L. 2005, *Instrument Science Report TEL 2005-02*, 23 pages, 2  
 Grillmair, C. J., Burrows, A., Charbonneau, D., et al. 2008, *Nature*, 456, 767  
 Hauschildt, P. H., Allard, F., & Baron, E. 1999, *ApJ*, 512, 377  
 Huitson, C. M., Sing, D. K., Vidal-Madjar, A., et al. 2012, *MNRAS*, 422, 2477  
 Huitson, C. M., Sing, D. K., Pont, F., et al. 2013, *MNRAS*, 434, 3252  
 Knutson, H. A., Charbonneau, D., Cowan, N. B., et al. 2009, *ApJ*, 690, 822  
 Knutson, H. A., Lewis, N., Fortney, J. J., et al. 2012, *ApJ*, 754, 22  
 Knutson, H. et al. 2014, *Nature*, 505, 66  
 Kreidberg, L. et al. 2014, *Nature*, 505, 69  
 Kreidberg, L. et al. 2014, *Science*, submitted  
 Lecavelier Des Etangs, A., Pont, F., Vidal-Madjar, A., & Sing, D. 2008, *A&A*, 481, L83  
 Lecavelier Des Etangs, A., Vidal-Madjar, A., Désert, J.-M., & Sing, D. 2008, *A&A*, 485, 865  
 Madhusudhan, N. 2012, *ApJ*, 758, 36  
 Madhusudhan, N., McCullough P. R., Crouzet, N., & Deming, D. 2014, *ApJ*, in press  
 Madhusudhan, N., & Seager, S. 2009, *ApJ*, 707, 24  
 Mandel, K., & Agol, E., 2002, *ApJ*, 580, L171.  
 Mandell, A. M., Haynes, K., Sinukoff, E., et al. 2013, *ApJ*, 779, 128  
 McCullough, P., & MacKenty, J. 2012, *Space Telescope WFC Instrument Science Report*, 8  
 McCullough, P. R., Berta, Z. K., Howard, A. W., MacKenty, J. W., & WFC3 Team 2012, *American Astronomical Society Meeting Abstracts #219*, 219, #241.14  
 McQuillan, A., Aigrain, S., & Roberts, S. 2012, *A&A*, 539, A137  
 McQuillan, A., Mazeh, T., & Aigrain, S. 2014, *ApJS*, 211, 24  
 Morley, C. V., Fortney, J. J., Kempton, E. M.-R., et al. 2013, *ApJ*, 775, 33  
 O'Neal, D., Neff, J. E., & Saar, S. H. 1998, *ApJ*, 507, 919  
 Pont, F., Gilliland, R. L., Moutou, C., et al. 2007, *A&A*, 476, 1347  
 Pont, F., Knutson, H., Gilliland, R. L., Moutou, C., & Charbonneau, D. 2008, *MNRAS*, 385, 109  
 Pont, F., Sing, D. K., Gibson, N. P., et al. 2013, *MNRAS*, 432, 2917  
 Rajan, A. et al. 2011, *WFC3 Data Handbook, HST Data Handbooks*,  
 Rayner, J. T., Cushing, M. C., & Vacca, W. D. 2009, *ApJS*, 185, 289  
 Seager, S., & Sasselov, D. D. 2000, *ApJ*, 537, 916  
 Sing, D. K., Désert, J.-M., Lecavelier Des Etangs, A., et al. 2009, *A&A*, 505, 891  
 Sing, D. K., Pont, F., Aigrain, S., et al. 2011, *MNRAS*, 416, 1443  
 Sing, D. K., Lecavelier des Etangs, A., Fortney, J. J., et al. 2013, *MNRAS*, 436, 2956  
 Stevenson, K. et al. 2014, *Science*, submitted  
 Swain, M. R., Vasisht, G., & Tinetti, G., 2008a, *Nature*, 452, 329.  
 Swain, M., Deroo, P., Tinetti, G., et al. 2013, *Icarus*, 225, 432  
 Swain, M. R., Line, M. R., & Deroo, P. 2014, *ApJ*, 784, 133  
 Tinetti, G., Vidal-Madjar, A., Liang, M.-C., et al. 2007, *Nature*, 448, 169  
 Tinetti, G., Deroo, P., Swain, M. R., Griffith, C. A., Vasisht, G., Brown, L. R., Burke C., & McCullough, P., 2010, *ApJ*, 712, L139.  
 Triaud, A. H. M. J., Queloz, D., Bouchy, F., et al. 2009, *A&A*, 506, 377  
 Wakeford, H. R., Sing, D. K., Deming, D., et al. 2013, *MNRAS*, 2223  
 Waldmann, I. P., Tinetti, G., Deroo, P., et al. 2013, *ApJ*, 766, 7



TABLE 1  
SUMMARY OF HST WFC3 OBSERVATIONS

HST Program (P.I.)	12881 (McCullough)
Number of HST orbits	5
Number of scans per orbit	16 Forward & 16 Reverse
Duration of scan (s)	5.97
Scan rate (arcsec s <sup>-1</sup> )[pixels s <sup>-1</sup> ]	(2.00)[16.5]
Peak signal on detector (electrons per pixel)	4.0 × 10 <sup>4</sup>
Grism (λλ)	G141 (1.1μm to 1.7μm)
Detector subarray size (pixels)	512x512
Sample sequence	RAPID
Samples per scan	8
Start of first scan (HJD)	2456448.983024
Corresponding planetary orbital phase	-0.09948
Start of last scan (HJD)	2456449.272364
Corresponding planetary orbital phase	0.03094

Notes: Forward and reverse scans were interleaved. Planetary orbital phase is defined to be zero at mid-transit.

TABLE 2  
LIGHT CURVE

EXPSTART MJD	EXPSTART HJD	Orbit	Scan	Sample	Flag	Counts	Flux
2456448.541735	2456449.044294	2	1	1	0	55426193	0.99996
2456448.541745	2456449.044304	2	1	2	0	55452872	1.00014
2456448.541755	2456449.044314	2	1	3	0	55434284	1.00011
2456448.541765	2456449.044324	2	1	4	0	55335761	0.99988
2456448.542414	2456449.044973	2	-1	3	0	61415662	0.99990
2456448.542424	2456449.044983	2	-1	4	0	61552322	1.00005
2456448.542434	2456449.044993	2	-1	5	0	61495951	0.99995
2456448.542444	2456449.045003	2	-1	6	0	61571866	1.00017
2456448.542454	2456449.045013	2	-1	7	0	61610879	1.00067
2456448.543054	2456449.045613	2	1	1	0	55466554	0.99990
2456448.543064	2456449.045623	2	1	2	0	55489200	0.99993

Notes: The printed table is a truncated version of the electronic table, to illustrate the format. Columns, left to right, are modified Julian date of the start of the exposure, the associated heliocentric Julian date, the HST orbit in the visit, the scan direction (1 = forward; -1 = reverse), the MULTIACCUM sample, a data-analysis flag, the total number of photoelectrons from HD 189733, and the associated normalized flux after detrending. Orbit 1 was not detrended and was ignored.

TABLE 3  
TRANSMISSION SPECTRUM

$\lambda$ ( $\mu\text{m}$ )	$\Delta R_p^2/R_s^2$ (ppm)	$\sigma$ (ppm)	Column	$\Delta R_p^2/R_s^2$ (ppm)	$\sigma$ (ppm)	$\Delta\Delta$ (ppm)
1.1279	-70	73	171.5	-58	55	-12
1.1467	15	67	175.5	-25	54	41
1.1655	46	105	179.5	36	53	9
1.1843	3	87	183.5	13	52	-9
1.2031	-71	80	187.5	-36	51	-35
1.2218	-77	70	191.5	-63	50	-14
1.2406	-148	56	195.5	-136	50	-11
1.2594	-32	62	199.5	-91	50	59
1.2782	-169	61	203.5	-108	50	-61
1.2970	-45	69	207.5	-21	49	-23
1.3157	-71	60	211.5	-86	49	15
1.3345	-50	66	215.5	20	49	-71
1.3533	102	55	219.5	106	49	-4
1.3721	117	61	223.5	75	49	42
1.3909	59	63	227.5	53	49	5
1.4096	183	77	231.5	195	49	-11
1.4284	167	64	235.5	165	50	2
1.4472	76	71	239.5	73	50	2
1.4660	-14	67	243.5	-41	50	26
1.4847	156	75	247.5	85	51	70
1.5035	-91	62	251.5	32	65	-123
1.5223	65	61	255.5	60	51	4
1.5411	-30	62	259.5	-53	52	22
1.5599	-22	72	263.5	-27	52	5
1.5786	68	87	267.5	61	53	7
1.5974	-69	75	271.5	12	54	-82
1.6162	-116	98	275.5	-111	55	-5
1.6350	30	84	279.5	-131	56	162

Notes. Units are as indicated; parts per million is abbreviated ppm. The tabulated uncertainties apply to the differential transit depths; an additional uncertainty applies to the overall depth - see text. The first three columns refer to the analysis of N. C.; Columns 5 and 6 refer to the analysis of D. D.; The last column contains the difference of the differential spectra, column 2 minus column 5.

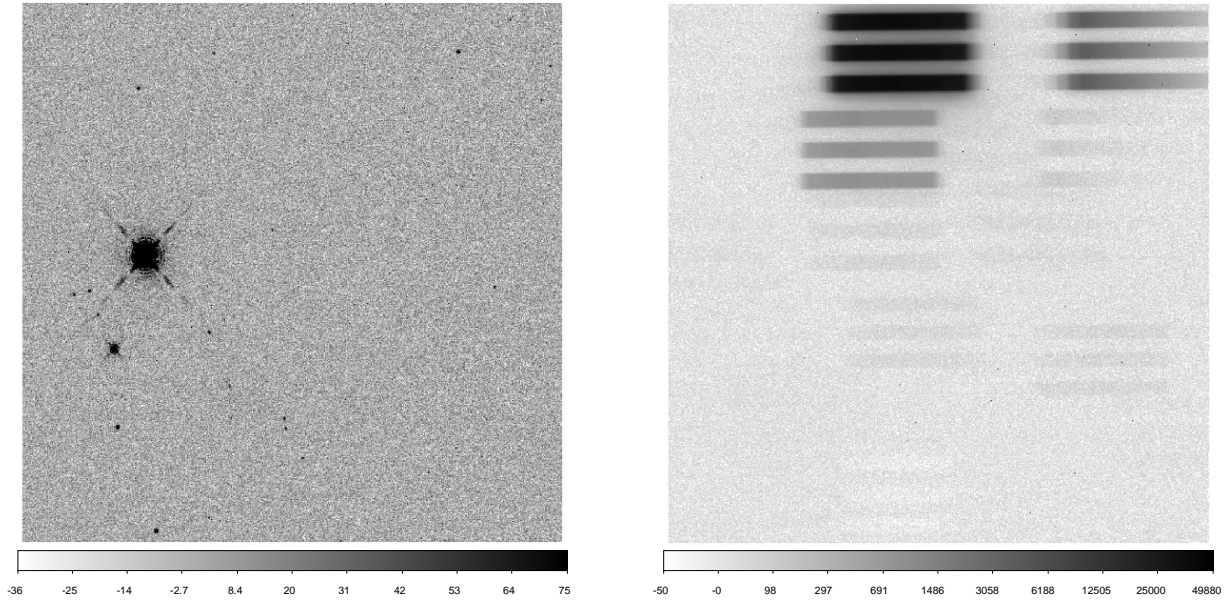


FIG. 1.— (Left) Direct image of HD 189733, from a 2.6-second exposure taken through filter F132N at the start of the visit. North is approximately to the right and East approximately up. The secondary star HD 189733B is at 7 o'clock with respect to the primary HD 189733A. We oriented HST so as to separate the two stars vertically on the detector in order to keep their two scanned spectra separate in our analysis. (Right) Scanned spectra of HD 189733. The orientation and pixel scale of this image are the same as the direct image. A logarithmic grey scale is indicated at the bottom in units of  $e^- \text{ pixel}^{-1}$ . For illustration purposes only, we numerically superposed three sub-exposures corresponding to the 3rd, 5th, and 7th differences between adjacent RAPID samples; the 4th and 6th differences (not shown) fill the gaps. Three first-order spectra of the primary star HD 189733A appear as black rectangles at middle top. Three first-order spectra of the secondary star HD 189733B appear in grey below the triad of primary star spectra. To the right of each first order spectrum, a corresponding 2nd order spectrum appears; they were not analyzed. With the 512 pixel by 512 pixel subarray and the selected sample sequence, each difference between samples corresponds to 0.853 s exposure and to 1.7 arcsec (14 pixels) vertically when scanned at  $2 \text{ arcsec s}^{-1}$ .

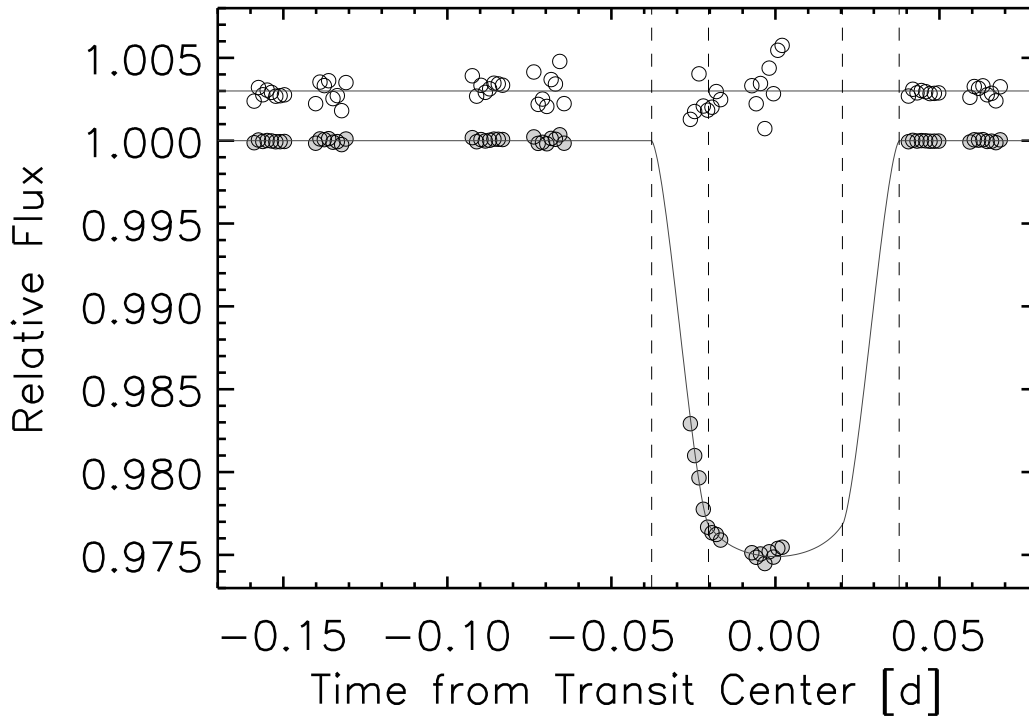


FIG. 2.— The white-light transit curve of HD 189733b, integrated over the WFC3 G141 bandpass with 0.8-second exposure per point. We obtained a total of nine such light curves, nearly simultaneously, via the MULTIACCUM samples of the detector. A limb-darkened transit model is overlaid (solid line) and the four planetary contacts are indicated (vertical dashed lines). Residuals have been expanded five-times in vertical scale and shifted above unity for clarity. Instrumental artifacts has been removed by fitting out-of-transit data (see text). The first HST orbit of the single visit is not shown.

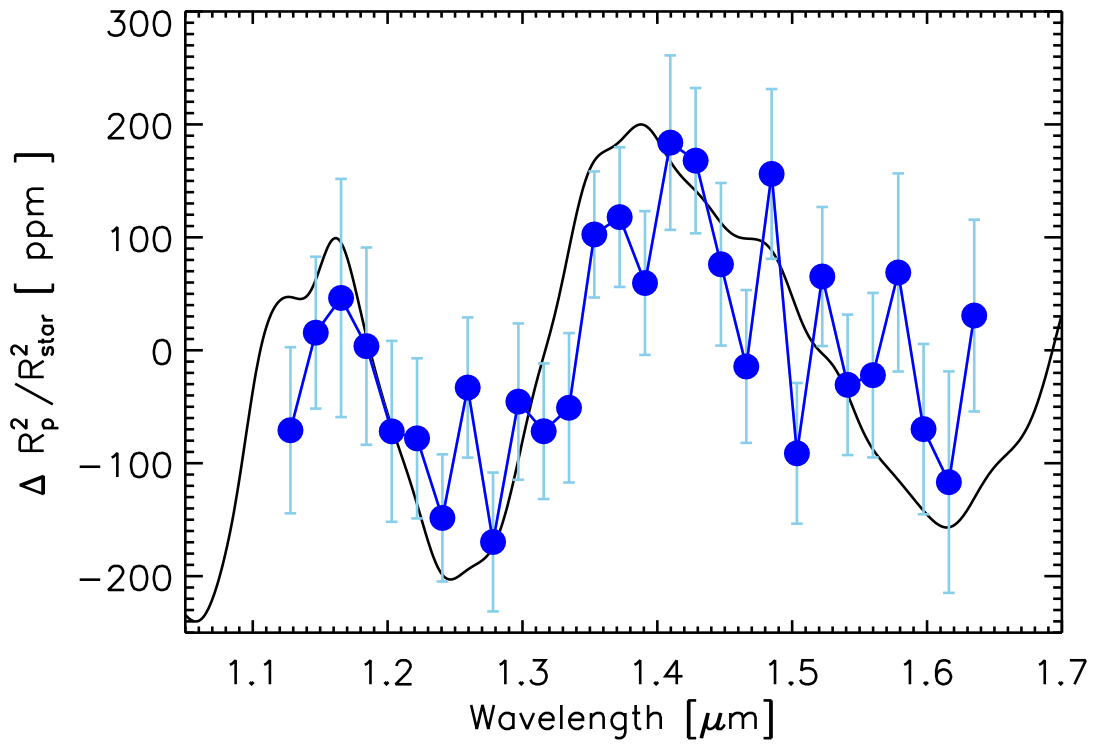


FIG. 3.— Transmission spectrum of the exoplanet HD 189733b compared to a theoretical model of a clear planetary atmosphere of solar composition. The model spectrum has a vast number of water vapor lines; for clarity the model spectrum has been Gaussian smoothed to FWHM=0.03  $\mu\text{m}$ .

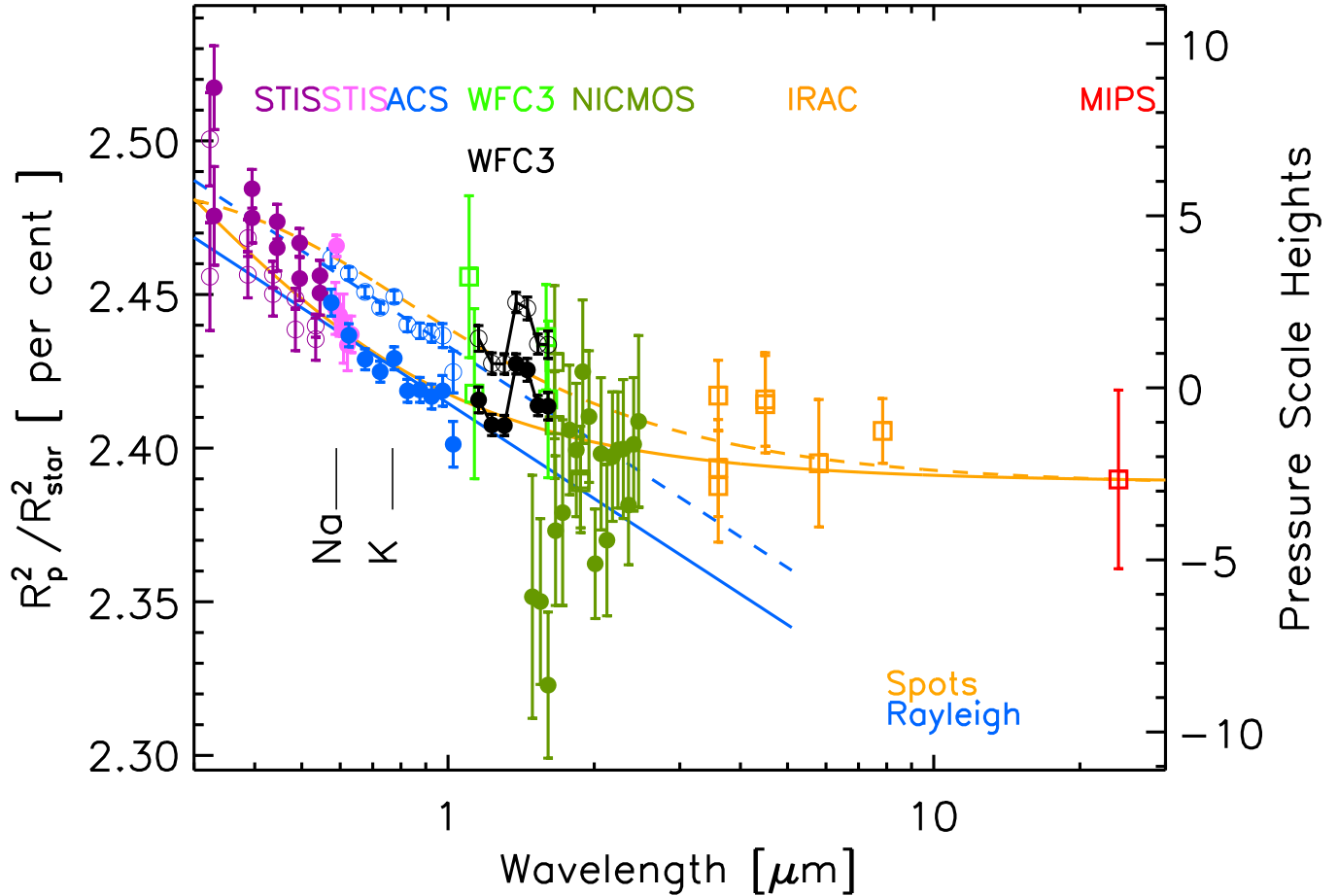


FIG. 4.— Transmission spectrum of the exoplanet HD 189733b. **Observations:** Data from Table 3 of this work, binned to seven points, are indicated by the filled black circles connected by a line. The WFC3 spectrum’s S-shaped undulation is attributed to water vapor (cf. Figure 5). Except for the WFC3 spectrum, all of the data and associated uncertainties are from Table 5 of Pont et al. (2013), including spectroscopy (filled colored circles) and photometry (open colored squares). As such, the illustrated NICMOS spectrum was reported originally by Gibson et al. (2011) and has a median uncertainty per point of 234 ppm. The median uncertainty per point estimated by three different analyses of those same NICMOS data ranges from 80 ppm to 234 ppm, although the shapes of the independently-derived spectra are similar (Swain et al. 2014). Data from Table 3 of Sing et al. (2011) include five pairs of points from the G430L grating of STIS (open violet circles), except their wavelengths have been reduced 2% for clarity. Data from Table 2 of Pont et al. (2008) include ten points from the G800L grating of ACS (open blue circles). Different corrections to the same data account for the different transit depths (open vs. filled circles;  $\lambda < 1.7\mu\text{m}$ ). Uncertainties are represented by  $1-\sigma$  error bars. Transitions of atomic sodium and potassium are indicated. **Models:** The blue dashed line is a fit to the Pont et al. (2008) data (open blue circles) by Lecavelier Des Etangs et al. (2008a) with a model of a clear, Rayleigh-scattering planetary atmosphere of the form of Eq. 1 of Lecavelier Des Etangs et al. (2008b). The blue solid line is the same fit, shifted down to match the data of Pont et al. (2013) (filled blue circles). The orange lines have a fixed planetary radius  $R_p$  and black-body stellar models with unocculted star spots. The temperature of the stellar photosphere is 5000 K. The modeled spot temperatures and covering fractions are 4600 K and 0.08 (solid), and 3700 K and 0.056 (dashed). Both spot models have been normalized at  $\lambda = 24\mu\text{m}$  to match the MIPS data point. An annulus of radius equal to  $R_p$  and width equal to a single  $T=1200$  K pressure scale height ( $H = 193$  km) corresponds to 112 ppm of transit depth, as indicated by the right scale.

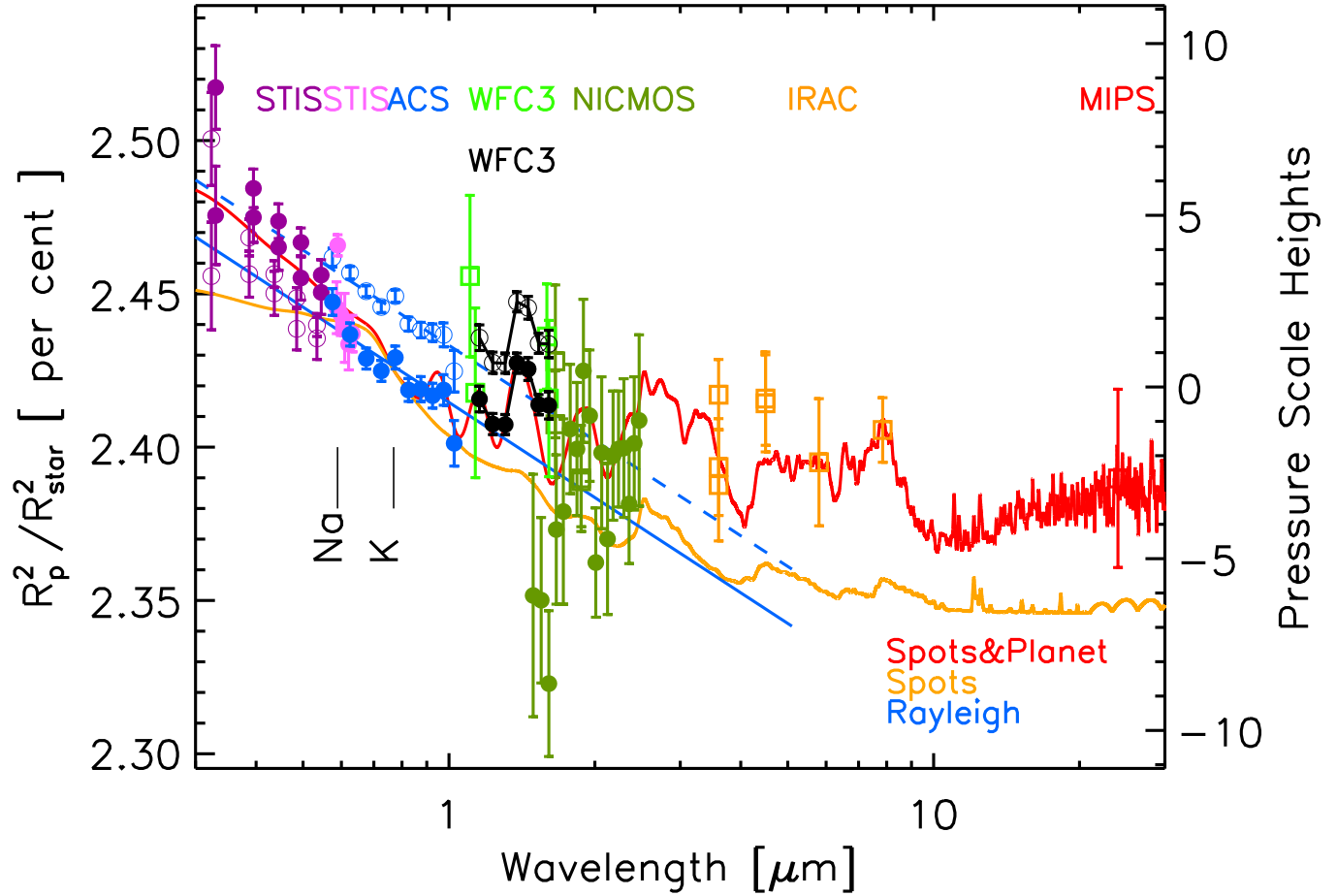


FIG. 5.— Transmission spectrum of the exoplanet HD 189733b. Same as Figure 4 except PHOENIX atmosphere models replace the black body models and the planetary radius  $R_p$  varies according to a physical model (see text). **Observations:** The upper WFC3 spectrum from our analysis (black open circles) is as-observed; the mean transit depth for the WFC3 data is approximately at the same level as the  $\sim 1 \mu\text{m}$  end of the ACS data (blue open circles) reported by Pont et al. (2008), which had been corrected for an assumed unocculted star spot level of 1%. The lower WFC3 spectrum (black filled circles) has been shifted down by 300 ppm to better match the ACS data (blue filled circles) corrected for an unocculted star spot level of 1.7% by Pont et al. (2013). **Models:** One model (upper, red line) combines two effects: 1) unocculted star spots with temperature  $T(\text{spot}) = 3700 \text{ K}$  and spot fractional area  $\delta = 0.056$ , and 2) a clear planetary atmosphere of solar composition, a mixing ratio for water of  $5 \times 10^{-4}$ , and zero alkali metal lines (Na and K) for a gas giant planet with physical parameters commensurate with HD 189733b. The other model (lower, orange line) is solely the contribution of the unocculted star spots of the first model. Both models have been smoothed with a Gaussian of  $\text{FWHM} = 0.089 \mu\text{m}$  for clarity.